Electrochemical behavior of in-situ electrosynthetized 3D metal-organic framework (MOF) as ultra-stable thin film on nickel foam

Thuan-Nguyen Pham-Truong, Hazar Guemiza, Hugo Lavillunière, Cedric Vancaeyzeele, Pierre-Henri Aubert

Electrochemical behavior of *in-situ* electrosynthetized 3D Metal-Organic Framework (MOF) as ultra-stable thin film on nickel foam

Thuan-Nguyen Pham-Truong,Hazar Guemiza, Hugo Lavillunière, Cedric Vancaeyzeele and Pierre-Henri Aubert*.*

CY Cergy Paris Université, LPPI, F-95000, Cergy.

Highlights

- A versatile approach was proposed to elaborate thin film of $Ni_3(HITP)_2$ metal organic framework at the surface of nickel foam
- As-prepared electrodes exhibits superior stability and electrochemical performance as binder free system
- Intensive electrochemical investigations were performed to get insight the understanding of the interface MOF/solution

Abstract: Metal-organic frameworks (MOFs) based materials have recently attracted a wide attention for developing of high-performing supercapacitors (SCs). In the present work, the $Ni_3(HITP)_2$ MOF was successfully electrosynthetized via a one-pot approach from and to the surface of nickel foam (NF) and served as ultra-stable thin film electrode. The presence of the active layer is evidenced by a wide range of technique ranging from morphological, spectroscopic to electrochemical ones. As the film was formed within the diffusion layer of the NF surface, the electrochemical accessible surface area was improved and the drawback of being low electrically conductive of MOF based materials could be minimized. Accordingly, it is confirmed by a significant charge accumulation over dissipation obtained by electrochemical impedance microscopy and a capacitance retention about 40 % from 0.01 to 10 $V.s^{-1}$. Besides, this approach allows the formed materials to be strongly attached to the surface of the current

⁎ Corresponding author at LPPI Laboratory, Chemistry Department, CY Cergy Paris Université, Neuville sur Oise, 95000 France

Email address: thuan-nguyen.pham-truong@cyu.fr (T-N. Pham-Truong); pierre-henri.aubert@cyu.fr (P-H. Aubert)

collector, thus significantly enhance the cycling stability around 100 % capacitance retention over 0.9 V for 170,000 cycles

Keywords. *Surface modification, metal-organic framework, electrochemistry, interface, thin film, supercapacitors*

1. Introduction

In contrast with battery systems, supercapacitor is dedicated to electrochemical storage system that stores electrical energy either by electrostatic absorption of ions within the electrochemical double layer (EDL) and/or rapid faradaic reactions coupled with fast ion insertion at the surface of materials. Indeed, the main difference between the two storage mechanisms results in no electron passing through the interface material/solution in the first configuration while in the latter situation, interfacial electron transfer occurs to change the redox-state of the active materials, leading to the contribution of pseudocapacitance, leading to high energy density[1–3]. From power density standpoint, electrochemical double layer capacitors (EDLC) outperforms others systems thanks to fast ion transport, *i.e*. commonly in the range of 10^{-6} - 10^{-8} $cm^2.s^{-1}$,[4] back and forth to the electrode surface. To achieve ultrahigh power density, the required materials, which are rarely found in the literature, must possess high electrochemical accessible surface area alongside with low electrical resistance. Up-to-date, a great majority of materials for EDLCs devices are mainly composed of carbon-based ones [5–7], e.g. activated carbon, CNTs, and graphene. Even though they possess high theoretical surface area, the experimental capacitance could not reach theoretical values, mainly due to severe problems[8–10], such as π-stacking, short/disordered ion-conduction channels, low packing density, etc. In parallel with the development of new synthetic procedure and/or processing methods using these materials, it is strongly expected to develop novel materials that could also satisfy the two crucial criteria. Indeed, a highly porous, additive-free and thin layer electrode with superior stability could response to all requirements.

In the last decade, metal organic frameworks (MOFs) have widely been investigated in a large range of applications thanks to their large specific surface area (~7,800 $m^2.g^{-1}$ up-to-date [11] and can further reach a theoretical value of ~15,000 $m^2.g^{-1}$) [12] as well as a capability to modulate the physical chemical properties by tuning their structure. Nevertheless, excepting few examples[13–17], pristine MOFs are rarely used in supercapacitor application, resulting mainly from their low electrical conductivity (< 10^{-2} $S.cm^{-1}$)[18]. In most reported works, MOFs were mainly used as: (1) precursors and/or template for generation of doped porous carbon by means of pyrolysis[19–21]; (2) constituent in composites by combining with other conductive materials, e.g. conducting polymers[22,23], carbon-based materials[24,25], etc. Even though high capacitances have been achieved, the cycling stability remains an important shortcoming for practical uses. As example, mixture of cobalt-based layered MOF, carbon

black and polytetrafluoroethylene (PTFE) binder exhibit extraordinary capacitance of 2474 $F.g^{-1}$@1 $A.g^{-1}$, the capacitance retention, therefore, decreases more than 5 % only after 2000 cycles[26]. For a wide skimming, Yaghi's group reported a series of 23 different MOF nanocrystals/graphene[27] with areal capacitance ranging from 0.221 to 5.085 $mF.cm^{-2}$. The cycling stability is strongly MOF-dependent, thus areal capacitance drop to 80% after 300 – 10,000 cycles. Recently, Dincă and colleagues reported the synthesis of two dimensional $Ni_3(HITP)_2$ (HITP = hexaiminotriphenylene) MOF that possess exceptionally high electrical conductivity (2 $S.cm^{-1}$ for bulk pellet, 40 $S.cm^{-1}$ for 500 nm-thick film[28] and up to 150 $S.cm^{-1}$ for single crystal[29]). It is worth noting that the bulk $Ni_3(HITP)_2$ MOF (pellet) owns a specific surface area (SSA) of 630 $m^2.g^{-1}$, leading to an obtained gravimetric capacitance of 111 $F.g^{-1}$ at discharge rate of 50 $mA.g^{-1}$. Accordingly, normalized capacitance of 18 $\mu F.cm^{-2}$ (polymeric binder and acetylene black free electrode) was achieved that outperforms most of carbon based materials and a strong cycling stability of 90 % in capacitance retention after 10,000 cycles at 2 $A.g^{-1}$. [16] Later, Nguyen et al.[17] reported the direct deposition of $Ni_3(HITP)_2$ MOF onto nickel foam by electrophoretic method, resulting to strongly bound MOF layer with 84% capacitance retention after 100,000 cycles and an areal capacitance of 15.69 $mF.cm^{-2}$@0.1 $mA.cm^{-2}$. However, the electrode has to be prepared via two-step process in which MOF materials must be solely prepared prior to the electrophoresis. Nevertheless, the fabrication of the electrode displays undoubtedly an important role in the performance of MOF materials.

We describe herein one-pot and *in-situ* functionalization of nickel surface with a thin layer of $Ni_3(HITP)_2$ through anodization of metallic nickel in presence of hexaaminotriphenylene (HATP) as novel approach to generate highly stable MOF attached layer (*Scheme 1*). As-prepared substrates can be directly used as thin film and additive-free electrode and exhibit extraordinary stable performance with negligible change in capacitance after being sonicated for 12 hours as well as a capacitance retention of about 100 % after 170,000 cycles. Moreover, owing properties of thin film system, the ion-diffusion kinetic is very fast, leading to a capacitance retention of about 50 % over a wide range of scan rate, i.e. from 10 $mV.s^{-1}$ to 10 $V.s^{-1}$ with an areal capacitance of 4.8 $mF.cm^{-2}$ at 10 $mV.s^{-1}$.

2. Experimental Methods

2.1 Chemicals. Triphenylene-2,3,6,7,10,11-hexaamine 6HCl (HATP.6HCl) was purchase from Shanghai Sunway Corp Ltd, Lithium perchlorate ($LiClO_4$, >99%), ammonia solution (28% wt.), potassium chloride (KCl, > 99%) were purchased from Sigma-Aldrich. All the chemicals were used as received without further purification.

2.2 Instrumentation. X-ray photoelectron spectroscopy (XPS) analysis were performed using a Thermo VG Scientific ESCALAB 250 system, fitted with a micro focused, monochromatic Al Kα (hν =

1486.6 eV). SEM images and EDXS were performed using a ZEISS GeminiSEM 300 and a Bruker Quantax 123 eV. Thermal gravimetric analysis (TGA) was performed using a TGA Q50 (TA INSTRUMENTS). The thickness of the substrate was recorded using a Dektak 150 (VEECO).

Electrochemical measurements were performed by using a Biologic VMP-3 potentiostat. For the electrosynthesis of NiMOF, nickel foam (NF) was used as working electrode (WE), graphite rod as counter electrode (CE) and Pt wire as quasi-reference electrode (QRE). For electrochemical characterization, nickel-based electrodes (A = 0.785 cm^2) were used as WE, activated carbon paste as CE (A = 0.785 cm^2) and Ag wire as QRE in a Swagelok three-electrode setup. For 2-electrode measurements, symmetrical Swagelok-type cell was performed by using 2 NiMOF@NF (A = 0.785 cm^2/disc) as active electrodes. The difference in choice of reference electrodes is to prevent interference of possible Ag contamination in presence of ammonia.

2.3 The electrosynthesis of $Ni_3(HITP)_2$ MOF was carried out in three-electrode cell in which a cleaned Ni foam (NF, 1 cm x 1 cm), graphite rod, Pt wire are used as working, counter, and reference electrodes (*Scheme 1*). They were immersed in 5 mL aqueous solution containing 1 mM of HATP.6HCl, 100 µL of ammonia solution (28 wt%) and 0.1 M of KCl. The anodization was performed by using chronoamperometry at different potentials during 1h (*Figure 1B and S2*). After electrodeposition, part

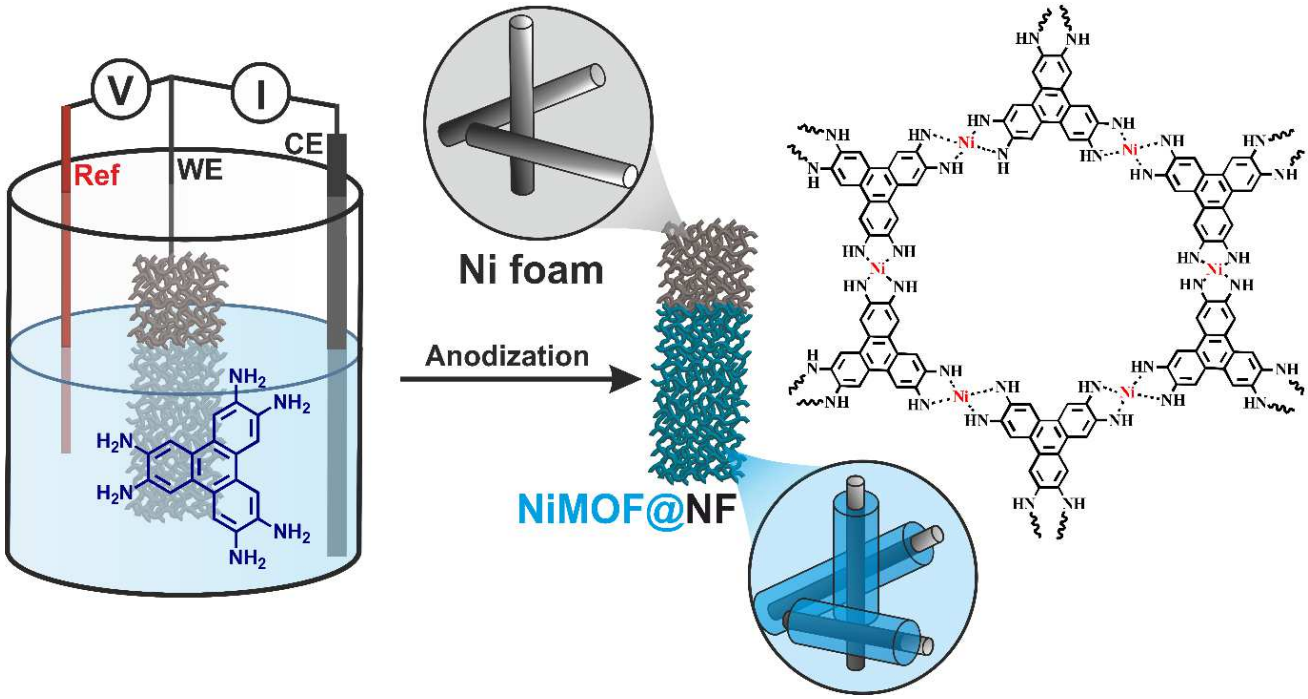

of deposited MOF was detached into the solution and form black precipitates, but a thin and uniform layer of Ni-MOF coats the surface of metallic nickel foam (*Figure 1B, inset*). Prepared Ni-MOF@NF substrates was washed thoroughly with distilled water, acetone followed by sonication for 30 minutes in a mixture of water/acetone (50:50 v/v). Afterwards, the substrates were dried and ready for use.

Scheme 1. Synthetic route for generation of 3D-thin film of $Ni_3(HITP)_2$ metal organic framework at the surface of nickel foam

3. Results and Discussion

3.1 Electrosynthesis of NiMOF.

To investigate the formation Ni-MOF at different applied potentials, 2 complementary techniques were used, i.e. cyclic voltammetry (CV) and chronoamperometry (CA). For CV, the potential was swept from -0.2 V to 1V/Pt QRE at a scan rate of 50 $mV.s^{-1}$ while for CA, fixed potentials were applied for 60 minutes. As displayed by the recorded voltammograms, different electrochemical coupled chemical processes could be observed. Indeed, the reaction follows two different electrochemical coupled chemical (EC) mechanisms in presence of ligand. The first EC pathway occurs at the potential range from 0 V to 0.4 V (*Figure 1A and inset*) where plateaus current is observed which corresponds to the formation of $Ni(II)_{ads}$ intermediates during the oxidation of $Ni(0) \rightarrow Ni(I)_{ads} \rightarrow Ni(II)_{ads} \rightarrow Ni^{2+}_{(sol)}$[30,31] followed

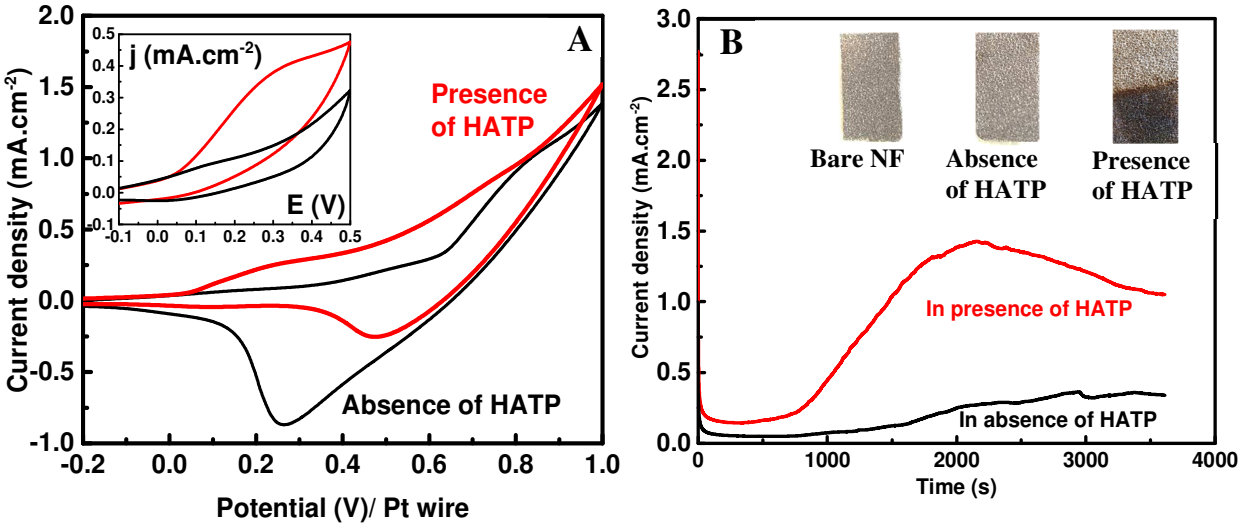

by the complexation with adsorbed HATP at the NF surface. Nevertheless, this pathway results to passivated thin layers of $Ni_3(HITP)_2$ that covers NF surface (See CA curves and SEM images at low potentials – *Figure S2 and 2A, respectively*). On the contrary, at higher potentials, the generation of $Ni^{2+}_{(sol)}$ ions in the diffusion layer becomes dominant and therefore, they react with the HATP at the vicinity of the surface, leading to formation of $Ni_3(HITP)_2$ clusters. Indeed, as displayed in the Figures 1A and S1, cyclic voltammogram of NF in HATP contained solution shows chemically irreversible electron transfer.

Figure 1. (A) Cyclic voltammograms of Ni foam (1 cm x 1 cm) in 5 mL aqueous solution containing 0.1 M of KCl, 100 µl of ammonia, in presence (*Red curve*, [HATP.6HCl] = 1 mM) or in absence (*black curve*) of HATP.6HCl, (inset) Zoomed

CVs from -0.1 V to 0.5 V; (B) Chronoamperometry curves at 0.45 V in presence and in absence of HATP, (*inset*) photos of nickel substrates (*from left to right*): Bare NF, modified nickel foam substrate in absence and in presence of HATP ligand, respectively. For all of the measurements, Pt wire was used as quasi-reference electrode.

Moreover, onset potential of oxidation to $Ni^{2+}_{(sol)}$ is observed at 0.55 V whilst the oxidation was shifted to lower onset value, i.e. E_{onset} = 0.3 V/ Pt wire in presence of HATP. The phenomenon could be attributed to a displacement of electron transfer equilibrium[32] due to the consumption of Ni^{2+} by complexing with amine groups. Due to π-stacking between $Ni_3(HITP)_2$ layers, the generated particles precipitate onto the surface of NF and further act as growing sites for formation of continuous MOF film with an estimated average thickness of about 150 nm, composed of small objects (d ~ 20 nm), that covers the whole surface of NF (*Figure 2B*). As presented in the Figure S11 A-D, the SEM and STEM images of detached NiMOF show tubular morphology over a thin carpet which an average length of 68 ± 20 nm and a diameter of 21 ± 5 nm which must be identical to the morphology of the attached NiMOF layer. Moreover, the specific surface area of the resulted material is calculated from BET measurements (Figure S11 E-F) to be at 350 $m^2.g^{-1}$ which an average pore size of ~ 2 nm which is similar to previously reported works[16,33]. Interestingly, upon deposition of Ni-MOF, the nickel surface is still electrochemically accessible with an increase in oxidative current (*Figure 1B and Figure S2A*). As observed by our experiments (Figure S2B), the performance of the substrate follows the CA's trend. Indeed, the achieved capacitance increases during the first 30 minutes deposition and reaches a saturation level thereafter. However, an excessive applied potential could lead to a domination of the second pathway, thus, generate larges and disordered precipitates (*Figure 2C*) causing electron transfer/ion transport blockage (*Figure S2*). In all cases, it was clearly evidenced that in presence of HATP ligand, the Ni-MOF was formed at the surface of the nickel foam.

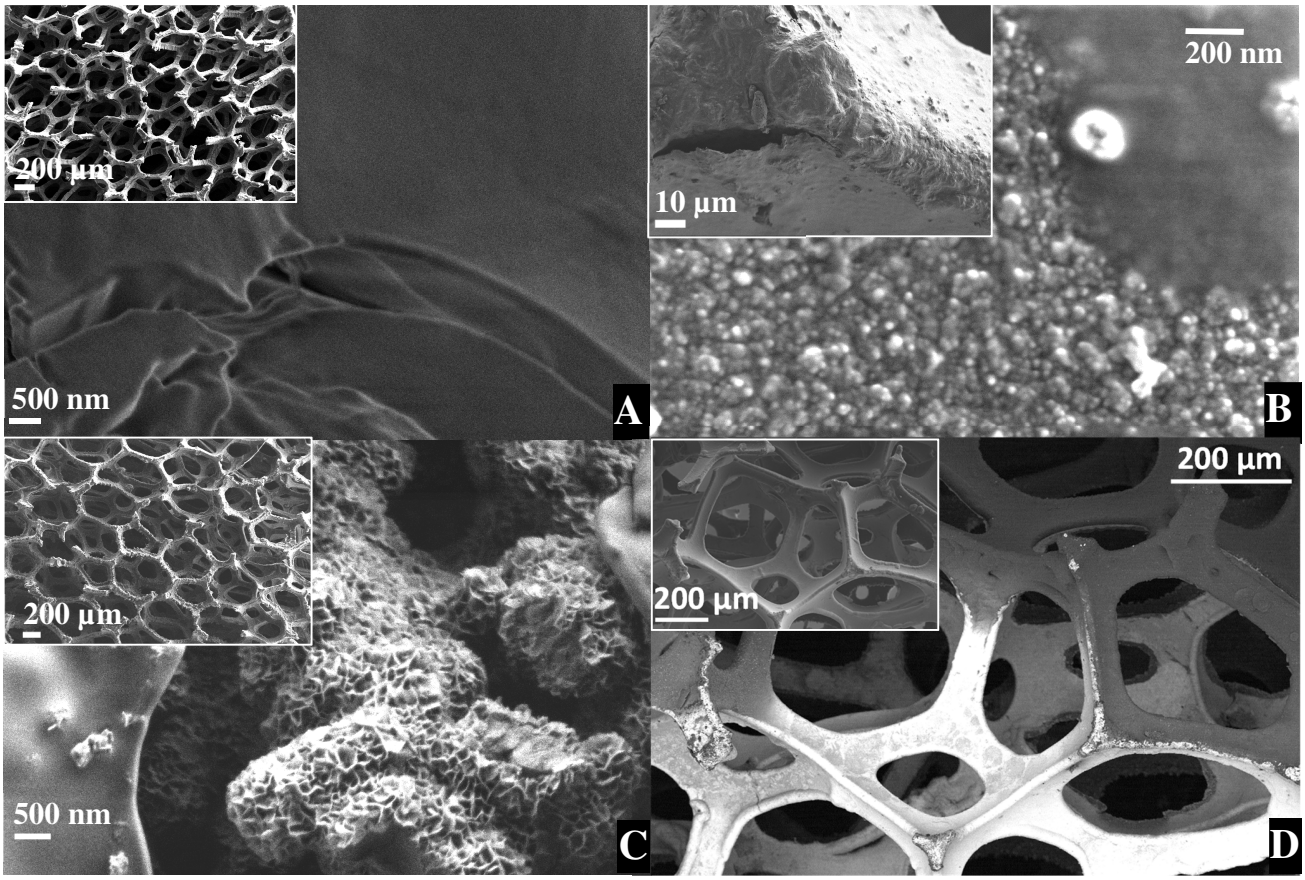

Figures 2. SEM images of NiMOF@NF prepared at (A) 0.2 V, (B) 0.45 V and (C) 0.55 V/Pt QRE as deposition potential by means of chronoamperometry in 5 mL aqueous solution containing 0.1 M of KCl, 100 µl of ammonia and 1 mM of HATP.6HCl, (D) BSD and (*inset*) SEM at low magnification image of sample prepared at 0.45 V.

From morphological standpoint, SEM images at low magnification show a uniform surface at nickel surface with no difference between the modified and non-modified regions (*Figure 2D*, *inset*), confirming that no change in macro-structure of nickel substrate upon the formation of Ni-MOF was detected. However, when backscattered electron detector (BSD) which detects elastically scattered electrons was used to probe the chemical environment of the substrate. Accordingly, difference in contrast appears as displayed in the Figure 2D. It should be noted that heavier elements are brighter in the recorded BSD image, corresponding to non-modified nickel surface, while in the other side, Ni atoms are, as expected with the formation of $Ni_3(HITP)_2$, diluted in carbon and nitrogen matrices, thus, a darker region is observed.

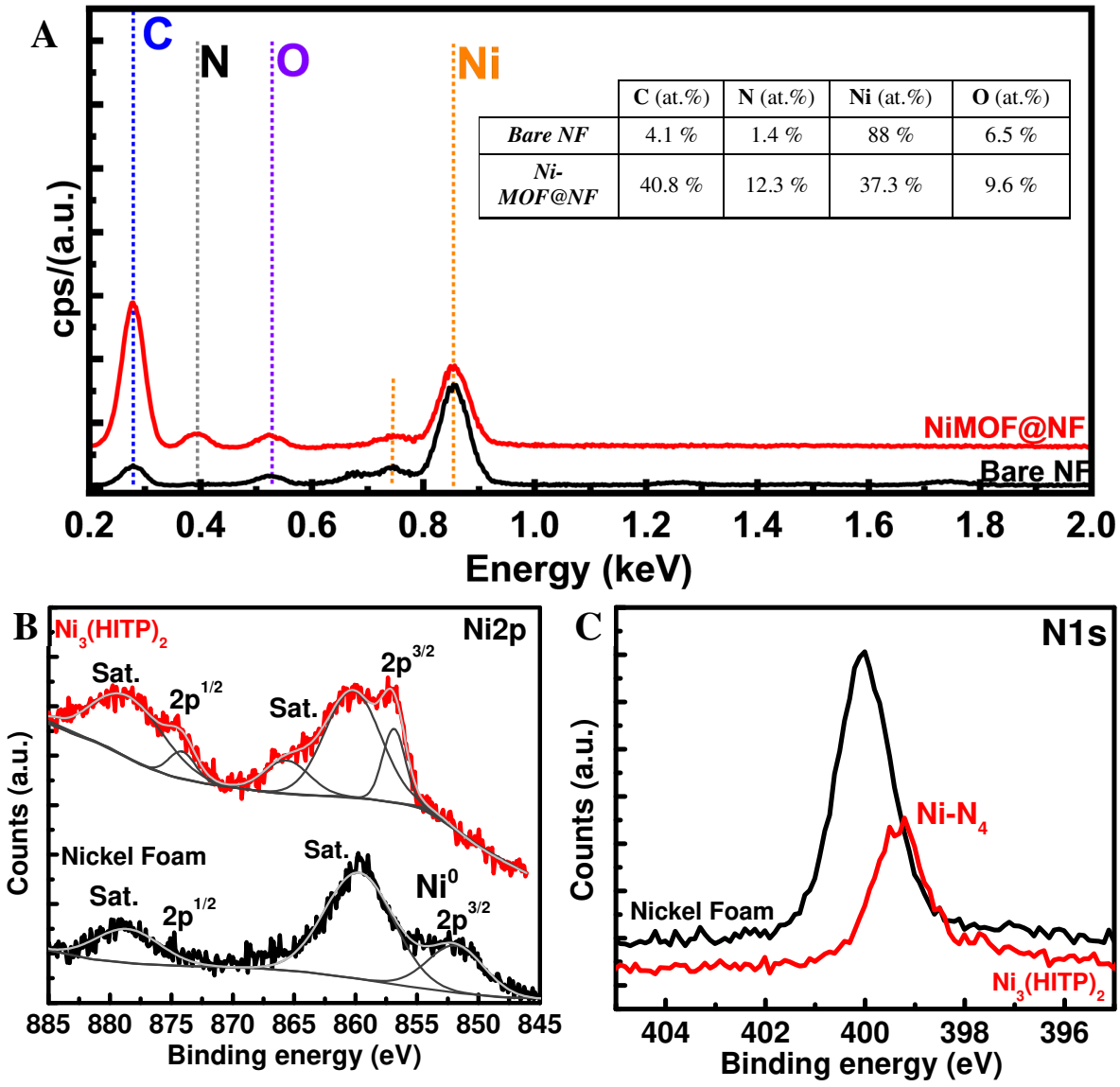

	C (at.%)	N (at.%)	Ni (at.%)	O (at.%)
Bare NF	4.1 %	1.4 %	88 %	6.5 %
Ni-MOF@NF	40.8 %	12.3 %	37.3 %	9.6 %

Figures 3. (A) EDX spectra of NF (black) and NiMOF@NF deposited at 0.45 V (red) and (*inset*) elemental composition; High-resolution XPS spectra of (B) Ni2p and (C) N1s.

To further confirm the presence of Ni-MOF layer at the surface, energy-dispersive X-ray spectroscopy (EDXS) was used, showing the presence of C (0.28 keV), N (0.39 keV), O (0.52 keV) and Ni (0.85 keV) as main elements for both sides. However, a decrease in Ni content (88 % vs. 37.3 %) as well as a

massive increase in carbon (4.1 % vs. 40.7 %) and nitrogen (1.42 % vs. 12.3 %) content was observed when passing from the bare Ni to Ni-MOF region, respectively (*Figure 3A*). Furthermore, the C/N ratio is about 3.3 which closely corresponds to the theoretical value of HATP ligand. In order to achieve more evidences in the formation of NiMOF, X-ray photoelectron spectroscopy (XPS) was used to probe the chemical composition.

From the survey spectra of $Ni_3(HITP)_2$ MOF@NF and non-modified NF, the presence of C1s, N1s, O1s and Ni2p can be confirmed for both samples which is consistent with EDX results (*Figure S3*). To get insight the chemical nature and environment of different elements, especially Ni2p and N1s, high resolution spectra were used as displayed in the Figure 3B-C. Two spin orbit peaks of Ni ($2p^{1/2}$ and $2p^{3/2}$) were observed at a binding energy of 874.1 and 856.9 eV which are similar to previously reported values[33]. Furthermore, single type of Ni peaks indicates the absence of potential oxide species (E_b = 853.7 – 855.9 eV)[34] generated during the anodization at the surface as well as good recovery of the NiMOF layer on top of metallic Ni foam (E_b = 852.1 eV). The formation of NiMOF at the surface can also be confirmed with the high-resolution spectra of N1s, showing Ni–N_4 type nitrogen at 399.1 eV[35] while nitrogen from contamination at the surface of nickel foam has to be located at around 400 eV.

Besides, the thermal stability of MOF layer was investigated via thermogravimetric measurements (*Figure S4A*), which showed no degradation at 350 – 500 °C as previously reported temperature for $Ni_3(HITP)_2$[33]. This phenomenon could be further explained by a low mass loading of Ni-MOF as well as a strong interaction between deposited layer and the substrate as already reported for other functionalized surface with thin-film systems[36,37].

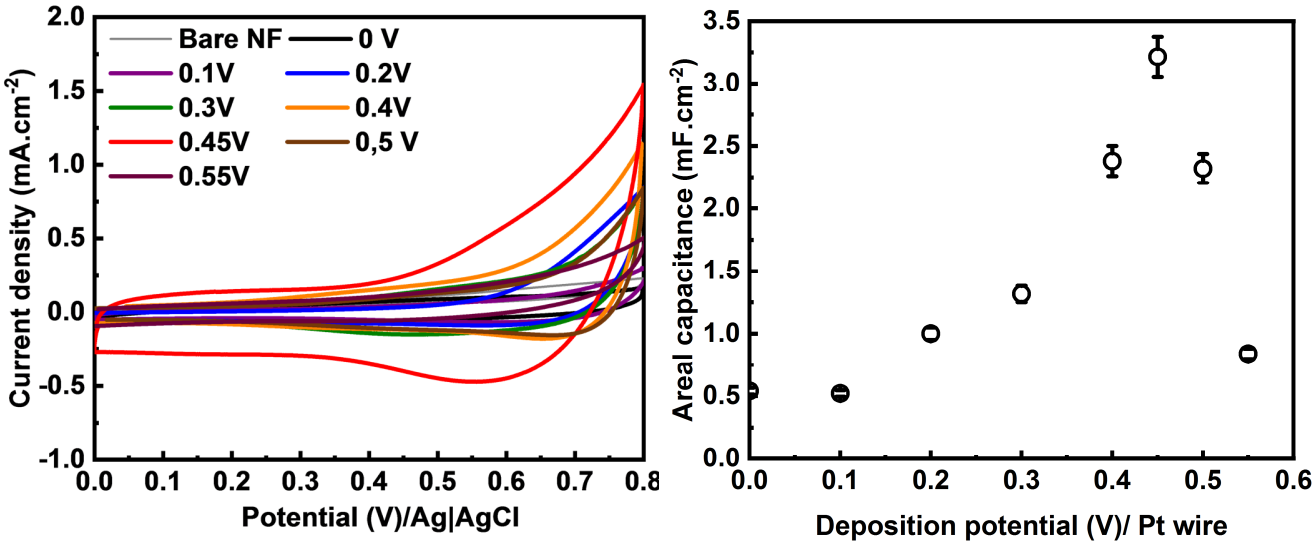

3.2 Electrochemical behaviors of Ni-MOF layer

Figures 4. (A) Cyclic voltammograms of electrodes prepared at different deposition potentials, ranging from 0V to 0.55 V/ Pt wire QRE, in aqueous solution containing 1 M of $LiClO_4$ at 50 $mV.s^{-1}$; (B) Calculated areal capacitance of the corresponding electrodes from CV curves.

For electrochemical behaviors of functionalized electrodes, cyclic voltammograms were recorded using electrodes prepared at different deposition potentials using 3-electrode setup (*Figure 4A*) and the areal capacitance was calculated and reported (*Figure 4B*). In all cases, the areal capacitances are enhanced, *i.e.* about 3 – 20 folds, comparing to bare nickel foam electrode, with an optimal value obtained with

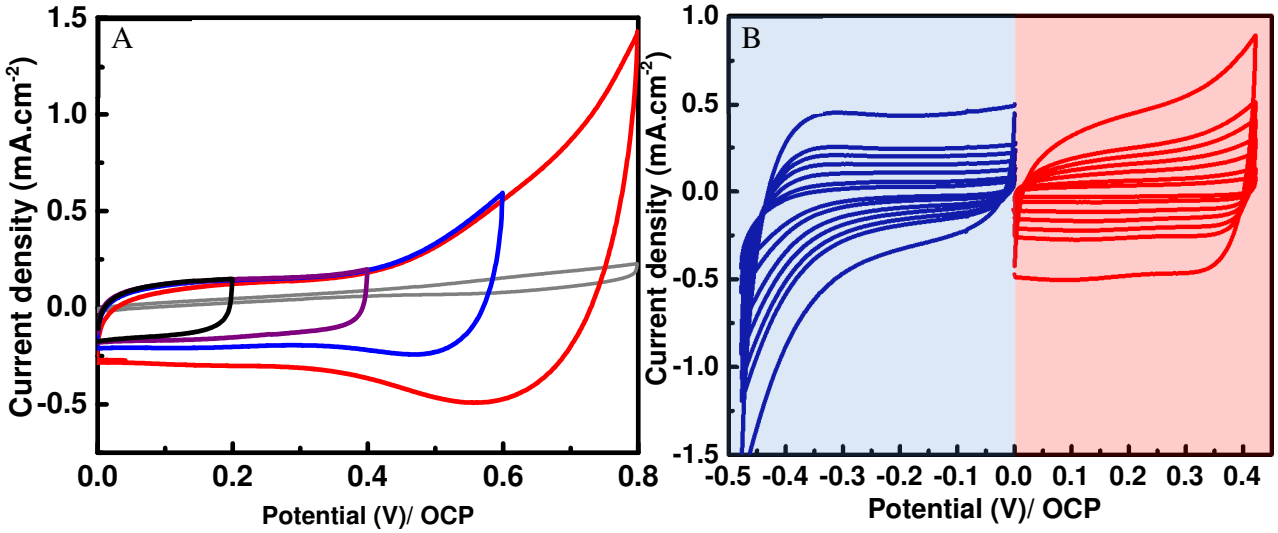

sample prepared at 0.45 V/Pt wire QRE. Accordingly, it is, again, confirmed about the presence of a thin porous layer of $Ni_3(HITP)_2$ metal organic framework.

Figures 5. (A) Cyclic voltammograms of NiMOF in different electrochemical windows at a scan rate of 50 $mV.s^{-1}$; (B) CVs at different scan rates (10, 20, 40, 60, 80, 100 and 200 $mV.s^{-1}$). All CV curves were recorded in aqueous solution containing 1 M $LiClO_4$. The measurements were performed using 3-electrode setup (WE = NF or NiMOF@NF, CE = Activated carbon, QRE = Ag wire).

Regarding the understanding of electrochemical phenomena at the interface between NiMOF@NF electrode and the electrolyte, voltammograms of optimized electrode at different electrochemical windows were recorded and shown in the Figure 5A. By increasing the swept potential range from 0.2 V to 0.8 V, faradaic current was observed at potentials beyond 0.5 V. Reversible redox couple at ~ 0.6 V could be attributed to the oxidation of open Ni^{2+} sites within MOF's structure to Ni^{3+}. Indeed, the observed phenomenon has already been reported by Dincă and coll.[38] by oxidizing Mn(II)-MOF-74 to Mn(III) in presence of iodobenzene dichloride. In order to evaluate the EDLC nature of the NiMOF layer, voltammograms at different scan rates were recorded from OCP to 0.4 V and to -0.5 V as shown in the Figure 5B. Linear dependence between current density and applied scan rate was obtained, resulting in a good rate capability of the electrode. Furthermore, the quasi-rectangular shape was maintained over a wide scan rate range (10 – 10,000 $mV.s^{-1}$, *Figure 5B and S5*), confirming the superior rate capability and demonstrating excellent electrostatic EDLC nature due to exceptional ion accessibility inside the porous layer. This characteristic is mainly observed in thin film electrode systems rather than with bulk

materials[39,40]. However, at a same value of scan rate, lower capacitive current was observed (*Figure 5B*) in the negative polarization (from 0V to – 0.3V/OCP), with $i_-/i_+ \sim 0.85$. It should be noted that the formation of Stern's double layer is strongly depended on the size of ions[41]. Thus, the aforementioned current ratio could be due to a larger hydrated ion size of Li^+ (0.382 nm) than of ClO_4^- (0.338 nm)[42]. Moreover, it is worth noting that further increase in applied potential would lead to the oxidation/reduction of electrolyte.

To get insight the electron transfer at the interface, electrochemical impedance spectra at different applied potentials were recorded and Nyquist plots over a frequency range from 100 kHz to 10 mHz are displayed in the Figure 6A. The Nyquist plots of the NiMOF sample remains similar with the applied potential, ranging from 0 to 0.8 V/OCP. Accordingly, the EIS spectra could be treated in 3 main regions. At high frequency (> 1 kHz), the plots intercept with the Z'-axis, resulting to a pure resistance behavior, represented as an equivalent series resistance (Z_{ESR}), which is mainly linked to the bulk electrolyte resistance ($Z_{ESR} \sim 1.1\ \Omega$). Conversely, in low frequency region (< 100 Hz), steep increase of the imaginary part (along Z"-axis) was observed which is linked to the electrostatic adsorption of ions in the porous MOF network. To evaluate the deviation from an ideal capacitor, constant phase element is used to extract the α-value ($0 < \alpha < 1$), which is depending on the diffusion of ion inside the pores of the electrode, according to the following formula[43]:

$$Z'' = \frac{1}{(j\omega C)^{\alpha}}$$

Two specific values of α could be expected: $\alpha = 0.5$ when the diffusive length (δ) is negligible compared to the electrode thickness (*e*) or semi-infinite Warburg law is validated and $\alpha = 1$ when the electrode behaves like a pure capacitor ($\delta = e$). Accurate α-value is therefore revealed as the slope of the $\log(Z'') = f(\log(\omega))$ plot and the evolution in function of applied potential is shown in the Figure 6B.

At potentials below 0.4 V, the values of α are close to 1 (0.8 – 0.92) which is typical for capacitive behavior. According to diffusion model inside porous materials reported by Cooper *et al.*[44] the porosity of the presented $Ni_3(HITP)_2$ layer is mainly composed of straight and closed pore which are coherently in adequation with its chemical structure. Beyond 0.4 V, α-values ~ 0.7 were obtained, indicating a significant resistance's contribution. Firstly, ionic resistance increases, resulting from a low ion mobility (in the range of 10^{-10} $cm^{-2}.s^{-1}$)[45] inside the porosity of the MOF in responding to the applied potentials. Indeed, the R_{ion} increases ~ 140 % (from 37 to 52 $\Omega.cm^{-2}$) as the potential increases from 0 V to 0.8 V. Secondly, as aforementioned, the open Ni(II) sites are susceptible for being electroactive which would undoubtedly increases the total resistance of the system. In contrast, NF only exhibits a very large charge transfer resistance, ranging from 2150 $\Omega.cm^{-2}$ @OCP to 166 $\Omega.cm^{-2}$ @0.8 V, which is due to the oxidation of Ni^0 in consistence with the corresponding α-values, ranging from 0.1 to 0.5 (*Figure 6B*).

Consequently, the NiMOF layer could not only induce a capacitive behavior to the electrode but also act as protecting layer against corrosion of metallic nickel under oxidative conditions (*Figure S6*). In order to access to the charge accumulation at the interface solid/electrolyte, complex capacitance was used. Indeed, charge accumulation and charge dissipation processes could be analyzed as real capacitance and imaginary capacitance, respectively, via below relationship [46]: $C(\omega) = C'(\omega) - jC''(\omega)$ where the real and imaginary capacitances are calculated by $C' = \frac{Z''(\omega)}{\omega\|Z(\omega)\|^2}$ and $C'' = -\frac{Z'(\omega)}{\omega\|Z(\omega)\|^2}$, respectively. Accordingly, the real capacitance could be considered as the storage capability of the system by means of charge accumulation at the interface electrode/electrolyte while the imaginary capacitance could, in contrast, be viewed as energy losses by dissipation, *e.g.* faradaic processes, self-discharge, etc.

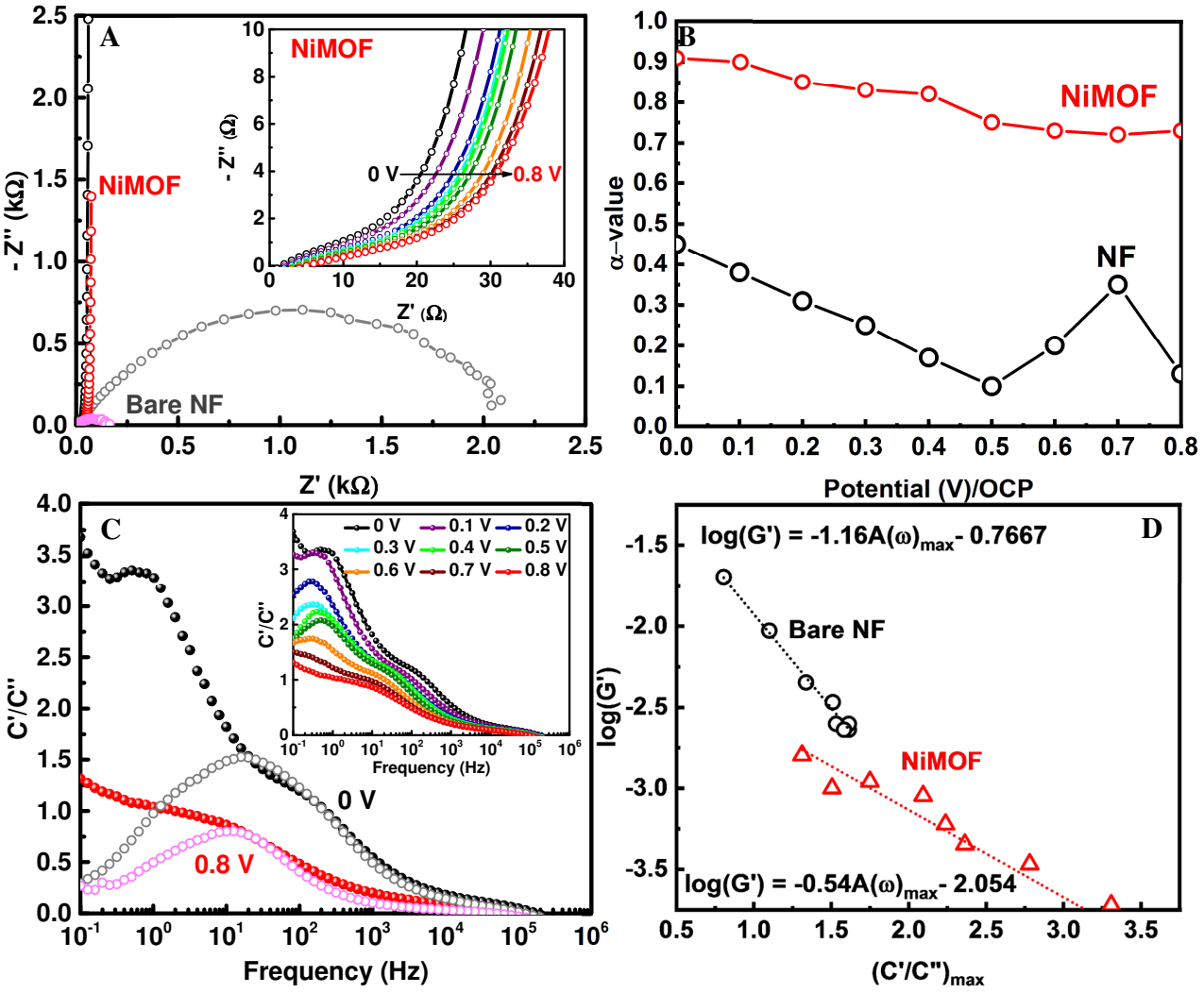

Figures 6. (A) EIS spectr□□t 0 V (gr□y □nd bl□ck) □nd 0.8 V (m□gent□ □nd red) of b□re NF □nd NiMOF, respectively; (*inset*) EIS spectr□of NiMOF b□sed electrode □t different potenti□ls, r□nging from 0 V to 0.8 V/OCP; (B) Evolution of α-v□lue in function of □pplied potenti□l for (Bl□ck) B□re NF □nd (Red) NiMOF@NF; (C) Corresponding dissip□tion r□tio; (*inset*) Dissip□tion r□tio of NiMOF@NF □t different potenti□ls □nd (D) Evolution of conduct□nce in function of □ccumul□tion r□tio's m□xim□for (red) NiMOF@NF □nd (bl□ck) B□re NF

As shown in the Figure S7, at high frequency (>> 10^2 Hz), both terms tend to zero-value which is attributed to high resistance behavior, inducing a difficulty for ions to be accumulated in the porosity of MOF's layer as well as for the charge to be dissipated. At lower frequency, an increase of both C' and C" is observed, indicating the beginning of both charge accumulation/dissipation. For charge accumulation (C'-term), by increasing the potential from 0 to 0.8 V/OCP, the onset frequency decreases from 126 to 1 Hz (*Figure S7A*). Thus, the system exhibits increasing resistance, resulting from low mobility of ion inside porous structure. Nevertheless, once all of ions are distributed in front of the pore surface, the formation of a compact ionic layer at the interface could be expected. Thus, an energy barrier is generated, allowing to slow down the ion dissipation as displayed by a decrease in C'' peaks with potential at ~ 6 Hz and ~ 0.15 Hz (*Figure S7B*). Consequently, the MOF system can undoubtedly provide high charge retention. As reference test, no significant change in onset frequency with applied potential under identical conditions was observed for bare nickel foam (*Figure S8*), indicating an absence in porous structure. In order to correlate the ratio between charge accumulation and dissipation process, accumulation ratio $A(\omega) = C'(\omega)/C''(\omega)$ is used. Accordingly, high value of $A(\omega)$ indicates the domination of charge accumulation at the surface. Consequently, $A(\omega)$ could be viewed as a key parameter instead of separately considering C' and C" to evaluate the interfacial phenomena in EDLC system. As displayed in the Figure 6C and S9, the accumulation ratio is plotted in function of the frequency in the log scale. For potential ranging from OCP to 0.8V and in the medium range in frequency, there is no difference between NiMOF and NF which is due to the domination of charge accumulation at the surface in both systems. However, at low frequency region, $A(\omega)$ continues to increase for NiMOF compared with NF substrate (*Figure S9*), indicating more and more charges are accumulated at in front of the active surface while the ratio decreases to zero in NF system, thus the oxidative charge consumption *via* nickel oxidation becomes dominant. However, the $A(\omega)$ peaks are shifted to lower frequencies as potential increases, corresponding to the left-shift in $C'(\omega)$ as aforementioned.

According to the works of Coster and colleagues[47] in the 90s on the use of complex conductance $G(\omega)$ in evaluation the boundary between electrode surface and electrolyte, the latter can be used to achieve a better understanding of the electron transfer through faradaic process and charge accumulation. Indeed, the intercept of the plot $\log(G'(\omega) = \omega C''(\omega)) = f(A(\omega)_{max})$ (*Figure 6D*) indicates the value of real conductance when charge dissipation becomes infinity. Accordingly, the G'-value for NiMOF is 8.9 mS while for bare NF substrate, a value of 171 mS, indicating that the electron transfer through faradaic processes is negligible for NiMOF compared to Bare NF, thus, confirming the role of the MOF layer to the protection of nickel surface towards corrosion as well as bringing new properties to the in-

terface, *i.e.* capacitive storage. Therefore, G'(ω) would also be an complementary parameter to investigate the kinetics of electrochemical processes at the interface of complex systems.

3.3 Application in supercapacitors

Towards application in supercapacitor devices, Swagelok cell with symmetrical 2-electrode setup in 1 M $LiClO_4$ electrolyte was used to evaluate the storage performance. Figure 7A – B show the voltammograms of the device at different scan rate, ranging from 10 $mV.s^{-1}$ to 10 $V.s^{-1}$, with a voltage of 0.9 V. All of recorded CV curves show quasi-rectangular shape, indicating superior capacitive behavior alongside with ultrahigh rate capability. As the mass of deposited NiMOF could not be determined with high accuracy, areal capacitance was calculated according to the following equation:

$$C_{areal} = \left(2\int idV\right) / \left(S \times \Delta V \times \nu\right)$$

where C_{areal} is the areal capacitance ($F.cm^{-2}$), $\int idV$ represents the area of the voltammogram, S (cm^2) the surface area of the electrode, ΔV (V) the operating voltage and ν ($V.s^{-1}$) the scan rate.

Thereinto, the areal capacitance of the $Ni_3(HITP)_2$ MOF@NF electrode is 4.8 $mF.cm^{-2}$ at 10 $mV.s^{-1}$ (Figure 7C) which is among highest reported values for additive/binder-free MOF systems towards supercapacitor application[17,48]. The total capacitance of the device is determined at 5 $mF.cm^{-2}$ basing on Trassatti'method which is composed of outer-pore capacitance of 0.85 $mF.cm^{-2}$ and of inner-pore capacitance of 4.15 $mF.cm^{-2}$ (*Figure S10*). Interestingly, the capacitance retention is remained about 40% as the scan rate increases by 1000-folds, *i.e.* 10 $V.s^{-1}$.

Actually, in thin-film systems, high electrical conductivity or low resistance from the electrode's materials is achieved. Indeed, high electron transport within the active layer could be expected, thus, the system is governed under ion-diffusion controlled regime. As the ion resistance is relatively low, the back and forth diffusion of electrolyte within the porosity of NiMOF is strongly enhanced in our configuration. Also, high capacitance retention is also an indication of highly ordered ion channels generated by the MOF's layer. Consequently, the NiMOF@NF system exhibits good performances with an energy density of 0.58 $\mu Wh.cm^{-2}$ at a power density of 0.05 $mW.cm^{-2}$ and the value remained at 0.22 $\mu Wh.cm^{-2}$@18.5 $mW.cm^{-2}$ which is comparable with other thin film systems[49–51].

Last but not least, $Ni_3(HITP)_2$ MOF@NF electrode exhibits superior stability over cycling in 1 M $LiClO_4$ aqueous electrolyte at 1 $V.s^{-1}$ using cyclic voltammetry (equiv. to 0.4 $mA.cm^{-2}$) as shown in the figure 7D. The symmetrical SC cell shows a capacitance retention of about 100% after 170,000 CV cycles. The slightly difference between the 1^{st} cycle and the $170{,}000^{th}$ one is attributed to the exposition of open Ni(II) sites to the solution, thus, increase in faradaic contribution (*Figure 7D, inset*). It should be noted that the extremely high adhesion of the attached layer is evaluated by sonication for overnight (~

12 hours). Even though the resistance is slightly increased, the areal capacitance is remained intact (*Figure S12*).

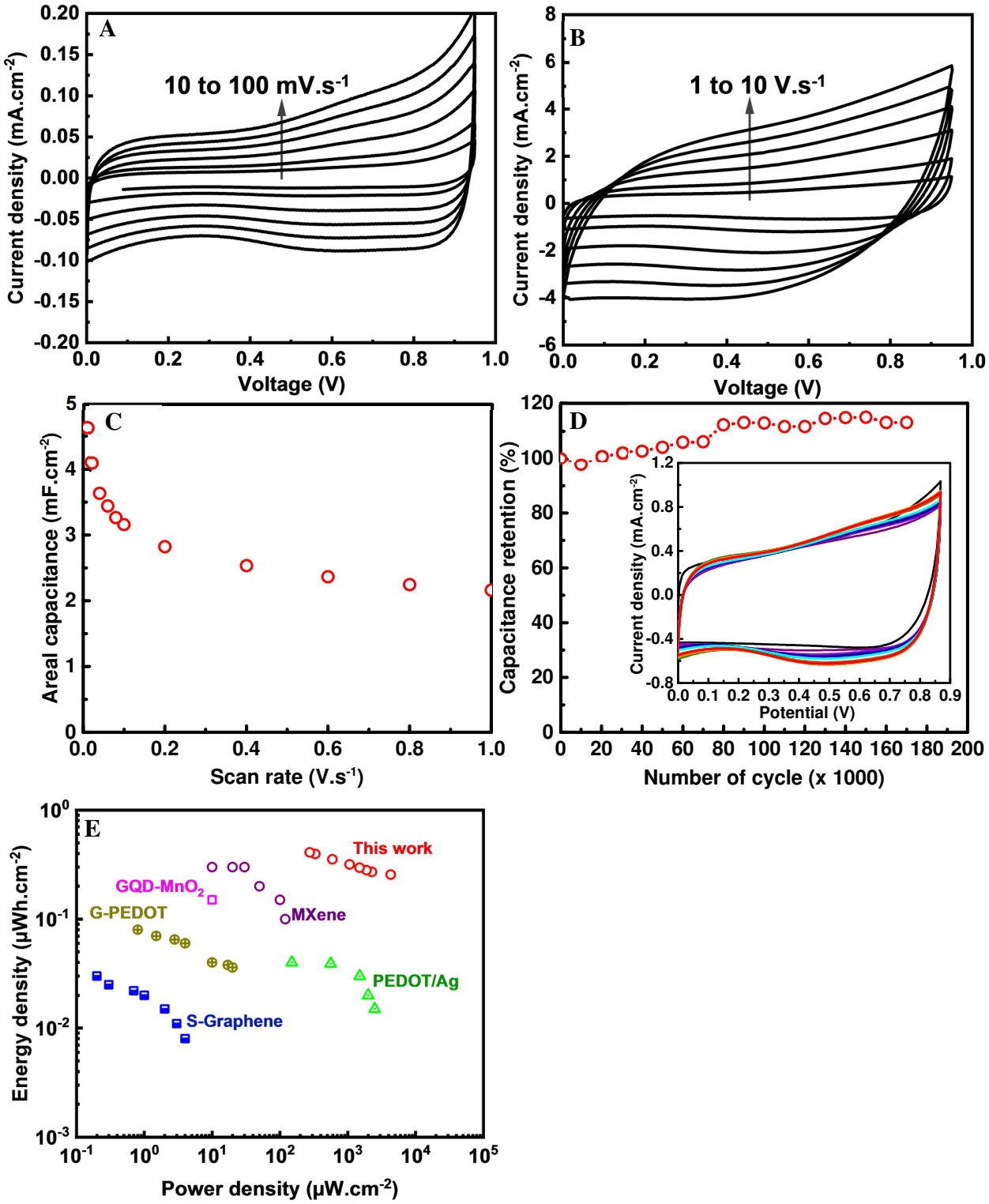

Figures 7. (A-B) CV at different scan rates of symmetrical 2 NiMOF electrodes; (C) Areal capacitance of symmetrical cell at different scan rates, (D) Capacitance retention after 170,000 cycles at 1 $V.s^{-1}$, (*inset*) Voltammograms at each 10,000 cycles using symmetrical cell and (E) Ragone plot presenting the performance of NiMOF system compared to others thin layer SCs[49–53]

4. Conclusions

In the present work, we have investigated the possibility to hierarchically and electrochemically generate $Ni_3(HITP)_2$ MOF thin film coated NF substrate by chemical reaction coupled electrochemical oxidation of metallic nickel substrate. The electrochemical behaviors of the formed surface were intensively investigated by different methods. Unlike bulk MOF's materials, the thin layer of metal organic framework exhibits very low electron transport resistance without using additives (e.g. carbon black and polymeric binder), thus minimizing surface-controlled process which is one of the major issues for application of MOF based materials in supercapacitor devices. From ion diffusion standpoint, even though the ion-resistance is relatively low, extended investigations are still required to tailor the pore structure as well as the chemical composition of the pore's wall in order to have a better ion diffusion and to lower ion trapping. In term of storage performance, the symmetrical cell exhibits an areal capacitance of 4.8 $mF.cm^{-2}$ at 10 $mV.s^{-1}$ which is among best performing additive-free MOF system up-to-date. Furthermore, this process could be easily upscaled by means of using a larger electrode or in a roll-to-roll process. However, different pathways could be explored to generate thin layers of MOF which are substrate-independent as well as to combine with other materials, *e.g.* conducting polymer. From different electrochemical characterization, $Ni_3(HITP)_2$ MOF presents a great promise in development of thin-film (micro)supercapacitor to power smart electronics.

CRediT authorship contribution statement. *Thuan-Nguyen Pham-Truong:* Conceptualization, methodology, Data acquisition, Analysis, Writing – Original draft; *Hazar Guemiza*: Data acquisition, Writing – Review & Editing; *Hugo Lavillunière*: Data acquisition, Writing – Review & Editing; *Cédric Vancaeyzeele*: Writing – review & editing, Investigation; *Pierre-Henri Aubert*: Writing – review & editing, Investigation

Data availability. Data will be made available on request.

Declaration of Competing Interest. The authors declare no conflict of interest.

Acknowledgment

The authors would like to thank the Conseil regional Île de France for funding the Cerasem project (grant:15013107) that has allowed the acquisition of a ZEISS Gemini SEM 300.

References

[1] A. Mohammadi Zardkhoshoui, B. Ameri, S.S. Hosseiny Davarani, A high-energy-density supercapacitor with multi-shelled nickel-manganese selenide hollow spheres as cathode and double-shell nickel-iron selenide hollow spheres as anode electrodes, Nanoscale. 13 (2021) 2931–2945. https://doi.org/10.1039/d0nr08234a.

[2] A. Mohammadi Zardkhoshoui, S.S. Hosseiny Davarani, M. Maleka Ashtiani, M. Sarparast, Designing an asymmetric device based on graphene wrapped yolk-double shell NiGa2S4 hollow microspheres and graphene wrapped FeS2-FeSe2 core-shell cratered spheres with outstanding

energy density, Journal of Materials Chemistry A. 7 (2019) 10282–10292. https://doi.org/10.1039/c9ta00532c.

[3] A. Mohammadi Zardkhoshoui, B. Ameri, S. Saeed Hosseiny Davarani, Fabrication of hollow MnFe2O4 nanocubes assembled by CoS2 nanosheets for hybrid supercapacitors, Chemical Engineering Journal. 435 (2022). https://doi.org/10.1016/j.cej.2022.135170.

[4] A.C. Forse, J.M. Griffin, C. Merlet, J. Carretero-Gonzalez, A.R.O. Raji, N.M. Trease, C.P. Grey, Direct observation of ion dynamics in supercapacitor electrodes using in situ diffusion NMR spectroscopy, Nature Energy. 2 (2017). https://doi.org/10.1038/nenergy.2016.216.

[5] L. Zhang, X.S. Zhao, Carbon-based materials as supercapacitor electrodes, Chemical Society Reviews. 38 (2009) 2520–2531. https://doi.org/10.1039/b813846j.

[6] T. Chen, L. Dai, Carbon nanomaterials for high-performance supercapacitors, Materials Today. 16 (2013) 272–280. https://doi.org/10.1016/j.mattod.2013.07.002.

[7] Y. Bin Tan, J.M. Lee, Graphene for supercapacitor applications, Journal of Materials Chemistry A. 1 (2013) 14814–14843. https://doi.org/10.1039/c3ta12193c.

[8] Y. Gogotsi, P. Simon, True performance metrics in electrochemical energy storage, Science. 334 (2011) 917–918. https://doi.org/10.1126/science.1213003.

[9] H.M. Cheng, F. Li, Charge delivery goes the distance, Science. 356 (2017) 582–583. https://doi.org/10.1126/science.aan1472.

[10] J. Ni, Y. Li, Carbon Nanomaterials in Different Dimensions for Electrochemical Energy Storage, Advanced Energy Materials. 6 (2016). https://doi.org/10.1002/aenm.201600278.

[11] I.M. Hönicke, I. Senkovska, V. Bon, I.A. Baburin, N. Bönisch, S. Raschke, J.D. Evans, S. Kaskel, Balancing Mechanical Stability and Ultrahigh Porosity in Crystalline Framework Materials, Angewandte Chemie - International Edition. 57 (2018) 13780–13783. https://doi.org/10.1002/anie.201808240.

[12] O.K. Farha, I. Eryazici, N.C. Jeong, B.G. Hauser, C.E. Wilmer, A.A. Sarjeant, R.Q. Snurr, S.T. Nguyen, A.Ö. Yazaydin, J.T. Hupp, Metal-organic framework materials with ultrahigh surface areas: Is the sky the limit?, Journal of the American Chemical Society. 134 (2012) 15016–15021. https://doi.org/10.1021/ja3055639.

[13] X. Zhao, K. Tao, L. Han, Self-supported metal-organic framework-based nanostructures as binder-free electrodes for supercapacitors, Nanoscale. 14 (2022) 2155–2166. https://doi.org/10.1039/d1nr08284a.

[14] W. Li, X. Zhao, Q. Bi, Q. Ma, L. Han, K. Tao, Recent advances in metal-organic framework-based electrode materials for supercapacitors, Dalton Transactions. 50 (2021) 11701–11710. https://doi.org/10.1039/d1dt02066h.

[15] D. Feng, T. Lei, M.R. Lukatskaya, J. Park, Z. Huang, M. Lee, L. Shaw, S. Chen, A.A. Yakovenko, A. Kulkarni, J. Xiao, K. Fredrickson, J.B. Tok, X. Zou, Y. Cui, Z. Bao, Robust and conductive two-dimensional metal-organic frameworks with exceptionally high volumetric and areal capacitance, Nature Energy. 3 (2018) 30–36. https://doi.org/10.1038/s41560-017-0044-5.

[16] D. Sheberla, J.C. Bachman, J.S. Elias, C.J. Sun, Y. Shao-Horn, M. Dincă, Conductive MOF electrodes for stable supercapacitors with high areal capacitance, Nature Materials. 16 (2017) 220–224. https://doi.org/10.1038/nmat4766.

[17] D.K. Ngyuen, I.M. Schepisi, F.Z. Amir, Extraordinary cycling stability of Ni3(HITP)2 supercapacitors fabricated by electrophoretic deposition: Cycling at 100,000 cycles, Chemical Engineering Journal. 378 (2019) 122150. https://doi.org/10.1016/j.cej.2019.122150.

[18] L.S. Xie, G. Skorupskii, M. Dincă, Electrically Conductive Metal-Organic Frameworks, Chemical Reviews. 120 (2020) 8536–8580. https://doi.org/10.1021/acs.chemrev.9b00766.

[19] C. Guan, X. Liu, W. Ren, X. Li, C. Cheng, J. Wang, Rational Design of Metal-Organic Framework Derived Hollow NiCo2O4 Arrays for Flexible Supercapacitor and Electrocatalysis, Advanced Energy Materials. 7 (2017) 1–8. https://doi.org/10.1002/aenm.201602391.

[20] Z. Xiao, Y. Mei, S. Yuan, H. Mei, B. Xu, Y. Bao, L. Fan, W. Kang, F. Dai, R. Wang, L. Wang, S. Hu, D. Sun, H.C. Zhou, Controlled Hydrolysis of Metal-organic Frameworks: Hierarchical Ni/Co-Layered Double Hydroxide Microspheres for High-Performance Supercapacitors, ACS Nano. 13 (2019) 7024–7030. https://doi.org/10.1021/acsnano.9b02106.

[21] C. Wang, C. Liu, J. Li, X. Sun, J. Shen, W. Han, L. Wang, Electrospun metal-organic framework derived hierarchical carbon nanofibers with high performance for supercapacitors, Chemical Communications. 53 (2017) 1751–1754. https://doi.org/10.1039/c6cc09832k.

[22] L. Wang, X. Feng, L. Ren, Q. Piao, J. Zhong, Y. Wang, H. Li, Y. Chen, B. Wang, Flexible solid-state supercapacitor based on a metal-organic framework interwoven by electrochemically-deposited PANI, Journal of the American Chemical Society. 137 (2015) 4920–4923. https://doi.org/10.1021/jacs.5b01613.

[23] J. Zhou, Y. Yuan, J. Tang, W. Tang, Metal-organic frameworks governed well-aligned conducting polymer/bacterial cellulose membranes with high areal capacitance, Energy Storage Materials. 23 (2019) 594–601. https://doi.org/10.1016/j.ensm.2019.03.024.

[24] P. Wen, P. Gong, J. Sun, J. Wang, S. Yang, Design and synthesis of Ni-MOF/CNT composites and rGO/carbon nitride composites for an asymmetric supercapacitor with high energy and power density, Journal of Materials Chemistry A. 3 (2015) 13874–13883. https://doi.org/10.1039/c5ta02461g.

[25] M. Saraf, R. Rajak, S.M. Mobin, A fascinating multitasking Cu-MOF/rGO hybrid for high performance supercapacitors and highly sensitive and selective electrochemical nitrite sensors, Journal of Materials Chemistry A. 4 (2016) 16432–16445. https://doi.org/10.1039/c6ta06470a.

[26] X. Liu, C. Shi, C. Zhai, M. Cheng, Q. Liu, G. Wang, Cobalt-Based Layered Metal-Organic Framework as an Ultrahigh Capacity Supercapacitor Electrode Material, ACS Applied Materials and Interfaces. 8 (2016) 4585–4591. https://doi.org/10.1021/acsami.5b10781.

[27] K.M. Choi, H.M. Jeong, J.H. Park, Y.B. Zhang, J.K. Kang, O.M. Yaghi, Supercapacitors of nanocrystalline metal-organic frameworks, ACS Nano. 8 (2014) 7451–7457. https://doi.org/10.1021/nn5027092.

[28] D. Sheberla, L. Sun, M.A. Blood-Forsythe, S. Er, C.R. Wade, C.K. Brozek, A. Aspuru-Guzik, M. Dincă, High electrical conductivity in Ni3(2,3,6,7,10,11- hexaiminotriphenylene)2, a semiconducting metal-organic graphene analogue, Journal of the American Chemical Society. 136 (2014) 8859–8862. https://doi.org/10.1021/ja502765n.

[29] R.W. Day, D.K. Bediako, M. Rezaee, L.R. Parent, G. Skorupskii, M.Q. Arguilla, C.H. Hendon, I. Stassen, N.C. Gianneschi, P. Kim, M. Dincă, Single Crystals of Electrically Conductive Two-Dimensional Metal-Organic Frameworks: Structural and Electrical Transport Properties, ACS Central Science. 5 (2019) 1959–1964. https://doi.org/10.1021/acscentsci.9b01006.

[30] A. Jouanneau, M. Keddam, M.C. Petit, A general model of the anodic behaviour of nickel in acidic media, Electrochimica Acta. 21 (1976) 287–292. https://doi.org/10.1016/0013-4686(76)80021-7.

[31] J. Gregori, J.J. García-Jareño, D. Giménez-Romero, F. Vicente, Kinetic calculations of the Ni anodic dissolution from EIS, Journal of Solid State Electrochemistry. 9 (2005) 83–90. https://doi.org/10.1007/s10008-004-0557-2.

[32] C. Sandford, M.A. Edwards, K.J. Klunder, D.P. Hickey, M. Li, K. Barman, M.S. Sigman, H.S. White, S.D. Minteer, A synthetic chemist's guide to electroanalytical tools for studying reaction mechanisms, Chemical Science. 10 (2019) 6404–6422. https://doi.org/10.1039/c9sc01545k.

[33] D. Sheberla, L. Sun, M.A. Blood-forsythe, S. Er, C.R. Wade, C.K. Brozek, A. Aspuru-Guzik, M. Dincă, High Electrical Conductivity in Ni3(2,3,6,7,10,11- hexaiminotriphenylene)2, a Semiconducting Metal−Organic Graphene Analogue, J. Am. Chem. Soc. 136 (2014) 8859–8862.

[34] W. Xing, S. Qiao, X. Wu, X. Gao, J. Zhou, S. Zhuo, S.B. Hartono, D. Hulicova-Jurcakova, Exaggerated capacitance using electrochemically active nickel foam as current collector in electrochemical measurement, Journal of Power Sources. 196 (2011) 4123–4127. https://doi.org/10.1016/j.jpowsour.2010.12.003.

[35] X.H. Liu, Y.W. Yang, X.M. Liu, Q. Hao, L.M. Wang, B. Sun, J. Wu, D. Wang, Confined Synthesis of Oriented Two-Dimensional Ni3(hexaiminotriphenylene)2Films for Electrocatalytic Oxygen Evolution Reaction, Langmuir. 36 (2020) 7528–7532. https://doi.org/10.1021/acs.langmuir.0c01128.

[36] M.Y. Gao, J.R. Zeng, Q.B. Zhang, C. Yang, X.T. Li, Y.X. Hua, C.Y. Xu, Scalable one-step electrochemical deposition of nanoporous amorphous S doped NiFe2O4/Ni3Fe composite films as highly efficient electrocatalysts for oxygen evolution with ultrahigh stability, Journal of Materials Chemistry A. 6 (2018) 1551–1560. https://doi.org/10.1039/c7ta08474a.

[37] I. Stassen, M. Styles, T. Van Assche, N. Campagnol, J. Fransaer, J. Denayer, J.C. Tan, P. Falcaro, D. De Vos, R. Ameloot, Electrochemical film deposition of the zirconium metal-organic framework uio-66 and application in a miniaturized sorbent trap, Chemistry of Materials. 27 (2015) 1801–1807. https://doi.org/10.1021/cm504806p.

[38] A.F. Cozzolino, C.K. Brozek, R.D. Palmer, J. Yano, M. Li, M. Dincai, Ligand redox non-innocence in the stoichiometric oxidation of Mn 2(2,5-dioxidoterephthalate) (Mn-MOF-74), Journal of the American Chemical Society. 136 (2014) 3334–3337. https://doi.org/10.1021/ja411808r.

[39] K. Kawashima, T. Ohnishi, K. Takada, High-Rate Capability of LiCoO2Cathodes, ACS Applied Energy Materials. 3 (2020) 11803–11810. https://doi.org/10.1021/acsaem.0c01973.

[40] J. Graetz, C.C. Ahn, R. Yazami, B. Fultz, Nanocrystalline and Thin Film Germanium Electrodes with High Lithium Capacity and High Rate Capabilities, Journal of The Electrochemical Society. 151 (2004) A698. https://doi.org/10.1149/1.1697412.

[41] I. Siretanu, D. Ebeling, M.P. Andersson, S.L.S. Stipp, A. Philipse, M.C. Stuart, D. Van Den Ende, F. Mugele, Direct observation of ionic structure at solid-liquid interfaces: A deep look into the Stern Layer, Scientific Reports. 4 (2014) 19–21. https://doi.org/10.1038/srep04956.

[42] C. Zhong, Y. Deng, W. Hu, J. Qiao, L. Zhang, J. Zhang, A review of electrolyte materials and compositions for electrochemical supercapacitors, Chemical Society Reviews. 44 (2015) 7484–7539. https://doi.org/10.1039/c5cs00303b.

[43] J. Segalini, B. Daffos, P.L. Taberna, Y. Gogotsi, P. Simon, Qualitative Electrochemical Impedance Spectroscopy study of ion transport into sub-nanometer carbon pores in Electrochemical Double Layer Capacitor electrodes, Electrochimica Acta. 55 (2010) 7489–7494. https://doi.org/10.1016/j.electacta.2010.01.003.

[44] S.J. Cooper, A. Bertei, D.P. Finegan, N.P. Brandon, Simulated impedance of diffusion in porous media, Electrochimica Acta. 251 (2017) 681–689. https://doi.org/10.1016/j.electacta.2017.07.152.

[45] P.J. Celis-Salazar, M. Cai, C.A. Cucinell, S.R. Ahrenholtz, C.C. Epley, P.M. Usov, A.J. Morris, Independent Quantification of Electron and Ion Diffusion in Metallocene-Doped Metal-Organic Frameworks Thin Films, Journal of the American Chemical Society. 141 (2019) 11947–11953. https://doi.org/10.1021/jacs.9b03609.

[46] H. Randriamahazaka, K. Asaka, Electromechanical analysis by means of complex capacitance of bucky-gel actuators based on single-walled carbon nanotubes and an ionic liquid, Journal of

Physical Chemistry C. 114 (2010) 17982–17988. https://doi.org/10.1021/jp106232s.

[47] H.G.L. Coster, T.C. Chilcott, A.C.F. Coster, Impedance spectroscopy of interfaces, membranes and ultrastructures, Bioelectrochemistry and Bioenergetics. 40 (1996) 79–98. https://doi.org/10.1016/0302-4598(96)05064-7.

[48] W. Zhao, T. Chen, W. Wang, B. Jin, J. Peng, S. Bi, M. Jiang, S. Liu, Q. Zhao, W. Huang, Conductive Ni3(HITP)2 MOFs thin films for flexible transparent supercapacitors with high rate capability, Science Bulletin. 65 (2020) 1803–1811. https://doi.org/10.1016/j.scib.2020.06.027.

[49] C. (John) Zhang, L. McKeon, M.P. Kremer, S.H. Park, O. Ronan, A. Seral-Ascaso, S. Barwich, C. Coileáin, N. McEvoy, H.C. Nerl, B. Anasori, J.N. Coleman, Y. Gogotsi, V. Nicolosi, Additive-free MXene inks and direct printing of micro-supercapacitors, Nature Communications. 10 (2019) 1–9. https://doi.org/10.1038/s41467-019-09398-1.

[50] S. Sollami Delekta, A.D. Smith, J. Li, M. Östling, Inkjet printed highly transparent and flexible graphene micro-supercapacitors, Nanoscale. 9 (2017) 6998–7005. https://doi.org/10.1039/c7nr02204b.

[51] W.W. Liu, Y.Q. Feng, X. Bin Yan, J.T. Chen, Q.J. Xue, Superior micro-supercapacitors based on graphene quantum dots, Advanced Functional Materials. 23 (2013) 4111–4122. https://doi.org/10.1002/adfm.201203771.

[52] Z.S. Wu, Z. Liu, K. Parvez, X. Feng, K. Müllen, Ultrathin Printable Graphene Supercapacitors with AC Line-Filtering Performance, Advanced Materials. 27 (2015) 3669–3675. https://doi.org/10.1002/adma.201501208.

[53] N. Kurra, B. Ahmed, Y. Gogotsi, H.N. Alshareef, MXene-on-Paper Coplanar Microsupercapacitors, Advanced Energy Materials. 6 (2016) 1–8. https://doi.org/10.1002/aenm.201601372.

Insert Table of Contents artwork here